

# First-principles calculation of the lattice thermal conductivities of $\alpha$ -, $\beta$ -, and $\gamma$ - $\text{Si}_3\text{N}_4$

Kazuyoshi Tatsumi,<sup>1,2,\*</sup> Atsushi Togo,<sup>2</sup> and Isao Tanaka<sup>2,3,4</sup>

<sup>1</sup>Advanced Measurement Technology Center, Institute of Materials and Systems for Sustainability, Nagoya University, Chikusa, Nagoya 464-8603, Japan

<sup>2</sup>Center for Elements Strategy Initiative for Structural Materials, Kyoto University, Sakyo, Kyoto 606-8501, Japan

<sup>3</sup>Department of Materials Science and Engineering, Kyoto University, Sakyo, Kyoto 606-8501, Japan

<sup>4</sup>Nanostructures Research Laboratory, Japan Fine Ceramics Center, Atsuta, Nagoya 456-8587, Japan

Lattice thermal conductivities of  $\alpha$ -,  $\beta$ - and  $\gamma$ - $\text{Si}_3\text{N}_4$  single crystals are investigated from *ab-initio* anharmonic lattice dynamics, within the single-mode relaxation-time approximation of the linearized phonon Boltzmann transport equation. At 300 K, the lattice thermal conductivity of  $\alpha$ - $\text{Si}_3\text{N}_4$  is calculated as  $\kappa_{xx} = 69$  and  $\kappa_{zz} = 99$  (in units of  $\text{Wm}^{-1}\text{K}^{-1}$ ). For  $\beta$ - $\text{Si}_3\text{N}_4$ ,  $\kappa_{xx} = 73$  and  $\kappa_{zz} = 198$  are obtained, that is consistent with the reported experimental values of 69 and 180, respectively. The difference of anisotropy between  $\alpha$ - $\text{Si}_3\text{N}_4$  and  $\beta$ - $\text{Si}_3\text{N}_4$  is originated from their characteristic difference in the phonon band structures, although their crystal structures are similar in their local atomic coordinates. In  $\alpha$ - $\text{Si}_3\text{N}_4$ , acoustic-mode phonons below 6 THz are the main heat carriers. In  $\beta$ - $\text{Si}_3\text{N}_4$ , the phonon modes up to 12 THz contribute to the lattice thermal conductivity. In  $\gamma$ - $\text{Si}_3\text{N}_4$ ,  $\kappa = 81$  is obtained. The distribution of phonon mode contributions to lattice thermal conductivity along phonon frequency is found to closely resemble  $\kappa_{xx}$  of  $\beta$ - $\text{Si}_3\text{N}_4$  although the phonon lifetimes of  $\gamma$ - $\text{Si}_3\text{N}_4$  are twice shorter than those of  $\beta$ - $\text{Si}_3\text{N}_4$ .

## I. INTRODUCTION

Several nitride insulators exhibiting good thermal conductivities are important for heat sink materials used at elevated temperatures. Wurtzite-type w-AlN, which has an Adamantine (diamond-like) crystal structure, was noted by Slack *et al.*<sup>1</sup> as a superior thermal conductor over 100  $\text{WK}^{-1}\text{m}^{-1}$ .  $\text{Si}_3\text{N}_4$  has been more recently recognized as one of the good thermally conductive insulators. Remarkable advances in ceramic technologies related to the densification of the sintered body and microstructural control have pushed the thermal conductivities of polycrystalline of  $\text{Si}_3\text{N}_4$  ceramics up to 177  $\text{WK}^{-1}\text{m}^{-1}$ .<sup>2-5</sup> Since  $\text{Si}_3\text{N}_4$  ceramics also exhibit high mechanical strength at elevated temperatures, they are regarded as ideal for use in various applications, such as engine components, gas turbines, and heat sink substrates of power semiconductor devices.

At atmospheric pressure,  $\text{Si}_3\text{N}_4$  exists in one of two phases,  $\alpha$  and  $\beta$ , both in the hexagonal lattice system, which are generally considered to be low- and high-temperature phases, respectively.<sup>2,5,6</sup> Their crystal structures are commonly formed by stacking of basal layers of  $\text{SiN}_4$  tetrahedra. The stacking manners in  $\alpha$  and  $\beta$ - $\text{Si}_3\text{N}_4$  are as ABCDABCD.. and ABAB.., respectively. This difference is depicted in Fig. 1 from the principal axis direction. The CD layers are related to AB by the c glide operation,<sup>7</sup> along which the unit cell periodicity of the  $\alpha$  phase is approximately two times longer than that of the  $\beta$  phase, with lattice constants of  $c = 5.62^8$  and  $2.91^9 \text{ \AA}$ , respectively. In addition to these phases, a cubic spinel phase ( $\gamma$ - $\text{Si}_3\text{N}_4$ ) can be formed upon compression and in-situ heating.<sup>10,11</sup> The reported transition pressures were scattered from 10 to 36 GPa depending on the experimental conditions. The produced  $\gamma$  phase

can be experimentally quenched to atmospheric pressure and room temperature.

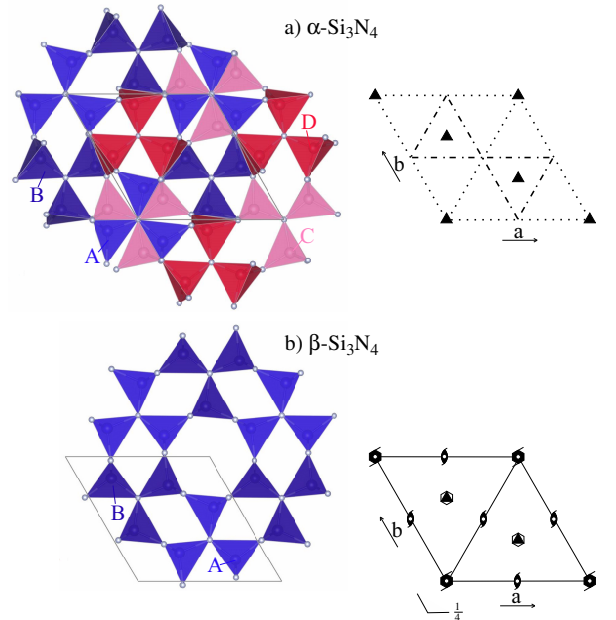


FIG. 1. (color online) Crystal structures of  $\alpha$ - and  $\beta$ - $\text{Si}_3\text{N}_4$ . Stacking of  $\text{SiN}_4$  tetrahedron layers are shown in left. (a) ABCDABCD.. for  $\alpha$ - $\text{Si}_3\text{N}_4$ . (b) ABAB.. for  $\beta$ - $\text{Si}_3\text{N}_4$ . Space group operations in  $P31c$  ( $\alpha$ - $\text{Si}_3\text{N}_4$ ) and  $P6_3/m$  ( $\beta$ - $\text{Si}_3\text{N}_4$ ) are shown in right.

By using high-resolution thermoreflectance microscopy, Li *et al.*<sup>12</sup> reported that the thermal conductivities of individual rod-shaped  $\beta$ - $\text{Si}_3\text{N}_4$  grains in a ceramic were 69 and 180  $\text{Wm}^{-1}\text{K}^{-1}$  along the  $a$

and  $c$  axes, respectively, and thus suggested the large anisotropy in thermal conductivity. Takahashi *et al.*<sup>13</sup> have recently developed a technique whereby  $\beta$ -Si<sub>3</sub>N<sub>4</sub> grains are coated with graphene of relatively high magnetic susceptibility, enabling them to align their  $c$  axes along the external magnetic field. Based on this technique, it has been proposed that the textural structure of rod-shaped  $\beta$ -Si<sub>3</sub>N<sub>4</sub> grains would increase their thermal conductivity to a level matching or exceeding that of w-AlN.

Although the fabrication of millimeter-sized  $\beta$ -Si<sub>3</sub>N<sub>4</sub> single crystals has been reported<sup>14</sup>, the thermal conductivity of no isolated single crystal of any Si<sub>3</sub>N<sub>4</sub> phase has yet been experimentally determined. It was proposed<sup>15</sup> that the anisotropy in the thermal conductivity of  $\beta$ -Si<sub>3</sub>N<sub>4</sub> phase grains may not stem from the intrinsic crystal properties, but rather, from the selective removal of crystal defects along the  $c$  axis of the grains. Theoretically, Hirosaki *et al.*<sup>16</sup> estimated the room-temperature lattice thermal conductivities (LTCs)  $\kappa_{xx}$  and  $\kappa_{zz}$  of  $\alpha$ -Si<sub>3</sub>N<sub>4</sub> to be 105 and 225 Wm<sup>-1</sup>K<sup>-1</sup>, and  $\kappa_{zz}$  of  $\beta$ -Si<sub>3</sub>N<sub>4</sub> to be 170 and 450 Wm<sup>-1</sup>K<sup>-1</sup>, respectively, by applying the Green-Kubo formulation to the molecular dynamics (MD) method with the interatomic potentials proposed by Vashishta *et al.* The ratio of the LTCs in the  $\beta$  phase along the  $a$  and  $c$  axes agreed well with the experimental results obtained by Li *et al.*; however, the absolute values were more than two times larger than the experimental results. The MD results suggest that the different stacking orders in  $\alpha$ - and  $\beta$ -Si<sub>3</sub>N<sub>4</sub> alter much their LTC, although the recent LTC calculation using first principles interatomic force constants (IFCs) has shown that in many polymorphs of the wurtzite and zincblende structures, which differ in terms of the stacking order of the densest atom planes as ABAB.. and ABCABC.., the stacking orders merely alter the LTCs.<sup>17</sup> For  $\gamma$ -Si<sub>3</sub>N<sub>4</sub>, its thermal conductivity has not been experimentally reported; it has been estimated only by the Slack model.<sup>18</sup> In short, while the thermal conductivity of polycrystalline  $\beta$ -Si<sub>3</sub>N<sub>4</sub> has been significantly improved<sup>2–5</sup>, our basic knowledge of, for example, the thermal conductivity tensors of the different Si<sub>3</sub>N<sub>4</sub> crystalline phases remains insufficient.

The present study aims to qualitatively understand the LTC tensors among the three Si<sub>3</sub>N<sub>4</sub> phases by means of the first principles approach. After the methodology section, we examine the validity of the present LTC results first. Then we investigate the characteristics in the LTCs in detail.

## II. COMPUTATIONAL PROCEDURES

### A. Lattice thermal conductivity calculation

The LTCs were calculated by solving the linearized Boltzmann transport equation (LBTE) within the single-mode relaxation time approximation (single-mode RTA).

We also tried the direct-solution of LBTE<sup>19</sup> and shortly leave its calculated LTC values in the following section. However the difference of LTCs between by the single-mode RTA and by the direct solution was found minor for our discussion. Therefore we limited our research based on the single-mode RTA to take advantage of the intuitive closed form of LTCs with the single-mode RTA. In the following sections, we denote a phonon mode by  $\lambda = (\mathbf{q}, p)$  by the set of the phonon wave vector  $\mathbf{q}$  and band index  $p$ . The relaxation time due to phonon-phonon scattering was obtained as reciprocal of linewidth,  $\tau_{\lambda,ph-ph} = (2\Gamma_{\lambda})^{-1}$ , where the linewidth that we employed in this study is as follows:

$$\begin{aligned} \Gamma_{\lambda} = & \frac{18\pi}{\hbar^2} \sum_{\lambda' \lambda''} |\Phi_{-\lambda \lambda' \lambda''}|^2 \times \\ & \{(n_{\lambda'} + n_{\lambda''} + 1)\delta(\omega_{\lambda} - \omega_{\lambda'} - \omega_{\lambda''}) + \\ & (n_{\lambda'} - n_{\lambda''})[\delta(\omega_{\lambda} + \omega_{\lambda'} - \omega_{\lambda''}) - \delta(\omega_{\lambda} - \omega_{\lambda'} + \omega_{\lambda''})]\}. \end{aligned} \quad (1)$$

Here  $\omega_{\lambda}$  is the harmonic phonon frequency of the phonon mode  $\lambda$ ,  $n_{\lambda} = [\exp(\hbar\omega_{\lambda}/k_B T) - 1]^{-1}$  shows the Bose-Einstein distribution at temperature  $T$ , and  $\Phi_{-\lambda \lambda' \lambda''}$  denotes the three-phonon-scattering strength.  $\Phi_{-\lambda \lambda' \lambda''}$  was obtained by usual coordinate transformation of third-order IFCs from direct space to phonon space.<sup>17</sup> The second- and third-order real-space IFCs were obtained from the ab-initio calculation, whose details are written in the next section.

In order to compare the more realistic results of the calculated LTC with the experimental data, the isotopic scattering effect due to the natural isotope distribution was taken into account according to the second-order perturbation theory.<sup>20</sup> With the relaxation times of the phonon-phonon scattering and isotropic scattering,  $\tau_{\lambda,ph-ph}$  and  $\tau_{\lambda,iso}$ , the total relaxation time for a phonon mode was assumed to be  $1/\tau_{\lambda} = 1/\tau_{\lambda,ph-ph} + 1/\tau_{\lambda,iso}$ , according to Matthiessen's rule.

These LTCs were calculated with the phonon-phonon interaction calculation code PHONO3PY<sup>17</sup>, while the harmonic phonon states were analyzed with the phonon calculation code PHONOPY<sup>21</sup>. These codes have been developed and maintained by the authors in this study.

The available experimental thermal conductivity data of the Si<sub>3</sub>N<sub>4</sub> system have been measured on the polycrystalline samples and not measured from any single crystals. In order to consider the effect of various lattice defects in the polycrystalline samples, such as grain boundaries, impurities, and vacancies, we crudely took them into account by a relaxation time  $\tau_{\lambda,bs} = L/|\mathbf{v}_{\lambda}|$  of a phonon boundary scattering model, where  $\mathbf{v}_{\lambda} = \nabla_{\mathbf{q}}\omega_{\lambda}$  is the group velocity and  $L$  a parameter regarding to the boundary mean free path. We consider  $\tau_{\lambda,bs}$  as a variable parameter and included it to LTCs according to Matthiessen's rule.

The closed form of the LTC tensors within RTA were

obtained via

$$\kappa(T) = \frac{1}{N_{\mathbf{q}}\Omega} \sum_{\lambda} \tau_{\lambda}(T) \mathbf{v}_{\lambda} \otimes \mathbf{v}_{\lambda} c_{\lambda}(T), \quad (2)$$

where  $N_{\mathbf{q}}$  is the number of  $\mathbf{q}$ -points,  $\Omega$  is the unit cell volume, and  $c_{\lambda}$  is the mode heat capacity. To analyze the LTC in detail, we calculate the cumulative thermal conductivity:

$$\kappa^c(\omega) = \frac{1}{N_{\mathbf{q}}\Omega} \int_0^{\omega} \sum_{\lambda} \tau_{\lambda}(T) \mathbf{v}_{\lambda} \otimes \mathbf{v}_{\lambda} c_{\lambda}(T) \delta(\omega' - \omega) d\omega'. \quad (3)$$

## B. Computational details

The IFCs were calculated using the first-principles projector augmented wave method<sup>22</sup> (VASP code<sup>23–25</sup>). The generalized gradient approximation (GGA) parameterized by Perdew, Burke, and Ernzerhof<sup>26</sup> was used for the exchange correlation potential. A plane wave energy cut-off of 500 eV was employed. The crystal structures were optimized until the convergence in the residual forces acting on the constituent atoms was less than  $10^{-6}$  eV/Å. The structural optimization was firstly performed for a temperature of 0 K and 0 GPa. Here the temperature and pressure were considered only for the electronic system and the zero point lattice vibration was not taken into account. The calculated lattice parameters were  $a = 7.808$  Å and  $c = 5.659$  Å for the  $\alpha$  phase,  $a = 7.660$  Å and  $c = 2.925$  Å for the  $\beta$  phase, and  $a = 7.787$  Å for the  $\gamma$  phase, which agree with the experimental data<sup>8,9,27</sup> within  $+0.7\%$  errors. The lattice volume optimized at 0 K and 0 GPa within the local density approximation (LDA)<sup>28</sup> for the exchange correlation potential was, for  $\beta$ -Si<sub>3</sub>N<sub>4</sub>, 3 % smaller than the volume with GGA, which is a typical volume contraction of LDA. In our test using  $\beta$ -Si<sub>3</sub>N<sub>4</sub> at 0 K and 0 GPa, the LTC calculated with LDA was larger by 2.6 % than that with GGA. For our discussion, these difference is enough small, therefore the impact of choice of exchange correlation potential is considered to be minor in our study.

Supercell and finite difference approaches were used to calculate the IFCs.<sup>29</sup> The  $1 \times 1 \times 2$ ,  $1 \times 1 \times 3$ , and  $1 \times 1 \times 1$  supercells of the conventional unit cells were adopted for the third-order IFCs of the  $\alpha$ ,  $\beta$ , and  $\gamma$  phases, respectively, while the larger supercells  $3 \times 3 \times 4$ ,  $3 \times 3 \times 8$  and  $2 \times 2 \times 2$  were adopted for the respective second-order IFCs. The constant atomic displacement distance was set to 0.03 Å. Table I shows the calculated LTC values for several different choices of supercell sizes, indicating that our calculated LTCs are reasonably converging with respect to the supercell sizes.

Uniform  $\mathbf{k}$ -point sampling meshes of  $4 \times 4 \times 2$ ,  $4 \times 4 \times 3$ , and  $3 \times 3 \times 3$  were used for the third-order IFCs of the  $\alpha$ ,  $\beta$ , and  $\gamma$  phases. For the former two phases the center of the  $a^*-b^*$  plane were sampled though the off-center

TABLE I. Calculated lattice thermal conductivities (LTC) of  $\alpha$ -,  $\beta$ -, and  $\gamma$ -Si<sub>3</sub>N<sub>4</sub> ( $\text{WK}^{-1}\text{m}^{-1}$ ) at 300 K with respect to several combinations of supercell sizes.

Phase	Supercell (# of atoms)		LTC	
	3 <sup>rd</sup> FC	2 <sup>nd</sup> FC	<i>xx</i>	<i>zz</i>
$\alpha$	1 $\times$ 1 $\times$ 1 (28)	1 $\times$ 1 $\times$ 1 (28)	37	57
	1 $\times$ 1 $\times$ 2 (56)	1 $\times$ 1 $\times$ 2 (56)	41	79
	1 $\times$ 1 $\times$ 1 (28)	2 $\times$ 2 $\times$ 2 (224)	56	81
	1 $\times$ 1 $\times$ 2 (56)	2 $\times$ 2 $\times$ 2 (224)	70	98
	1 $\times$ 1 $\times$ 2 (56)	2 $\times$ 2 $\times$ 3 (336)	69	97
	1 $\times$ 1 $\times$ 2 (56)	3 $\times$ 3 $\times$ 4 (1008)	69	99
$\beta$	1 $\times$ 1 $\times$ 2 (28)	1 $\times$ 1 $\times$ 2 (28)	40	166
	1 $\times$ 1 $\times$ 2 (28)	2 $\times$ 2 $\times$ 4 (224)	75	208
	1 $\times$ 1 $\times$ 3 (42)	2 $\times$ 2 $\times$ 4 (224)	71	194
	1 $\times$ 1 $\times$ 3 (42)	2 $\times$ 2 $\times$ 5 (280)	72	197
	1 $\times$ 1 $\times$ 3 (42)	3 $\times$ 3 $\times$ 8 (1008)	73	198
$\gamma$	1 $\times$ 1 $\times$ 1 (56)	1 $\times$ 1 $\times$ 1 (56)		75
	1 $\times$ 1 $\times$ 1 (56)	2 $\times$ 2 $\times$ 2 (448)		81
	1 $\times$ 1 $\times$ 1 (56)	3 $\times$ 3 $\times$ 3 (56)		82

grids along  $c^*$ -axis were sampled. For the  $\gamma$  phase, non- $\Gamma$  center mesh was used. For the second-order IFC, the  $\Gamma$ -point was only sampled for the  $\alpha$  and  $\beta$  phase supercells and the only one  $\mathbf{k} = (0.5, 0.5, 0.5)$  point was sampled for the  $\gamma$  phase supercell. The  $\mathbf{q}$ -point sampling meshes of  $10 \times 10 \times 14$ ,  $10 \times 10 \times 26$ , and  $12 \times 12 \times 12$  were used to calculate the LTCs in Eq. (2) for the  $\alpha$ ,  $\beta$ , and  $\gamma$  phases.

To compare the calculated LTC with the experimental data measured at finite temperatures, the experimentally measured lattice parameters may be preferred in case that they are known. We examined LTC of  $\beta$ -Si<sub>3</sub>N<sub>4</sub> at the equilibrium volumes ( $V_{\text{eq}}(T)$ ) within the quasi-harmonic approximation (QHA).<sup>30</sup> Except for this, the LTC values were calculated with the equilibrium volume at 0 K ( $V_{\text{eq}}(T = 0)$ ).

We calculated volumetric thermal expansion coefficients and compared them with the reported experimental values so as to check the validity of the present calculation, because the thermal expansion is originated from the anharmonicity of the interatomic potential as well as lattice thermal conduction. The calculated values are  $4.31$  and  $4.19$  ( $10^{-6}$  K $^{-1}$ ) at 300 K for the  $\alpha$  and  $\beta$  phases, while the experimental values were  $3.75$  and  $3.55$  ( $10^{-6}$  K $^{-1}$ )<sup>31</sup>. The present calculation reproduced the experimental tendency where the  $\alpha$  phase has a slightly larger thermal expansion coefficient than the  $\beta$  phase, supporting that the present calculations enable us to qualitatively compare the LTC values of the Si<sub>3</sub>N<sub>4</sub> phases.

In order to compare the microscopic phonon properties among the three phases at the same conditions, those results calculated at 0 GPa are shown and discussed. For the  $\gamma$  phase, this means that we assume the condition of virtually quenched  $\gamma$  phase at 0 GPa from the high pressure. To examine this, we calculated LTC of  $\gamma$  phase

at 10, 20, and 40 GPa as shown in Fig. 6, where the phenomenological behaviour of linear dependence of LTC with respect to pressure with the calculated slope of  $2.89 \text{ Wm}^{-1}\text{K}^{-1}\text{GPa}^{-1}$  was reproduced as similar to ref. 32. By this result, we consider that the microscopic values are also varied smoothly with the pressure and those at 0 GPa are meaningful to compare with the  $\alpha$  and  $\beta$  phases.

### C. Direct solution of LBTE

The merit of the single-mode RTA is that we can intuitively understand the qualitative character of LTC in terms of the relaxation time and group velocity. The microscopic understanding of the full solution of LBTE is still under the development<sup>33</sup> and the microscopic picture based on collective phonons<sup>34</sup>) will require more complicate investigation although it is known that the single-mode RTA solution of LBTE underestimates the full solution.<sup>35,36</sup>

For the  $\alpha$  and  $\beta$  phases, we partly adopted a direct solution of LBTE<sup>19</sup>, which is one of the methods of LBTE full solutions. The LTC values of the direct solution without the isotope effect were 69 and  $102 \text{ WK}^{-1}\text{m}^{-1}$  for  $\kappa_{xx}$  and  $\kappa_{zz}$  of the  $\alpha$  phase and 76 and 238 for those of the  $\beta$  phase, respectively, while the corresponding single-mode RTA values were 70 and  $102 \text{ WK}^{-1}\text{m}^{-1}$  for the  $\alpha$  phase and 76 and  $210 \text{ WK}^{-1}\text{m}^{-1}$  for the  $\beta$  phase. The  $\kappa_{zz}$  of the direct solution in the  $\beta$  phase was 13 % larger than that of the single-mode RTA solution. Since the LTC difference between the LBTE solutions is not significant and we expect the physics on LTC is well understood within RTA in the current level of our interest.

## III. RESULTS AND DISCUSSION

### A. Lattice thermal conductivities

In Table II, the theoretical LTCs at 300 K are compared with the previously reported experimental<sup>5,12,37,38</sup> and theoretical<sup>16–18</sup> values. The present calculation results better agree with the experimental  $\kappa_{xx}$  and  $\kappa_{zz}$  of  $\beta\text{-Si}_3\text{N}_4$ , compared with the references of the Slack model<sup>18</sup> and MD<sup>16</sup> results. The directional averages of the present in the  $\alpha$ ,  $\beta$ , and  $\gamma$  phases are 79, 115, and 81  $\text{Wm}^{-1}\text{K}^{-1}$ . The value of the  $\gamma$  phase is just as small as that of the  $\alpha$  phase, although the former phase shows the largest bulk modulus ( $B$ ) in Table II. It is generally known that simple models through Debye temperature can provide only their rough estimations.

It can be seen that the theoretical LTCs of  $\beta\text{-Si}_3\text{N}_4$  are markedly more anisotropic than those of the  $\alpha$  phase. The theoretical LTCs of  $\beta\text{-Si}_3\text{N}_4$  are in good agreement with the corresponding experimental data for individual grains reported by Li *et al.*<sup>12</sup>, indicating that the experimentally reported large anisotropy in the thermal conductivities of  $\beta\text{-Si}_3\text{N}_4$  stems from the intrinsic properties

TABLE II. Calculated thermal conductivities of  $\alpha\text{-Si}_3\text{N}_4$  (trigonal),  $\beta\text{-Si}_3\text{N}_4$  (trigonal),  $\gamma\text{-Si}_3\text{N}_4$  (cubic), and wurtzite-type AlN (hexagonal) at 300 K, compared with the experimental data. Theoretical bulk moduli  $B$  in units of GPa, calculated by the authors by using the present band method, are presented in the fourth column.

	This work			Ref. Theo.		Ref. Expt.		
	$\kappa_{xx}$	$\kappa_{zz}$	$B$	$\kappa$	$\kappa_{xx}$	$\kappa_{zz}$	$\kappa$	$\kappa_{xx}$
$\alpha\text{-Si}_3\text{N}_4$	69	99	224	70 <sup>a</sup>	105 <sup>b</sup>	225 <sup>b</sup>	59 <sup>d</sup>	-
$\beta\text{-Si}_3\text{N}_4$	73	198	237	250 <sup>a</sup>	170 <sup>b</sup>	450 <sup>b</sup>	122 <sup>e</sup>	69 <sup>f</sup>
$\gamma\text{-Si}_3\text{N}_4$	82	-	296	80 <sup>a</sup>	-	-	-	-
w-AlN	218	190	196	-	240 <sup>c</sup>	212 <sup>c</sup>	285 <sup>g</sup>	-

<sup>a</sup> Ref. 18, Slack model

<sup>b</sup> Ref. 16, molecular dynamics (Green-Kubo)

<sup>c</sup> Ref. 17, LBTE full solution.

<sup>d</sup> Ref. 37, thin film.

<sup>e</sup> Ref. 5, poly-crystals.

<sup>f</sup> Ref. 12, single crystalline grains of poly-crystals.

<sup>g</sup> Ref. 38, single-crystal.

of the crystal, rather than specific defects induced during the sample preparation process. Among the nitrides studied, the theoretical LTC of  $\beta\text{-Si}_3\text{N}_4$  along the c axis ( $194 \text{ Wm}^{-1}\text{K}^{-1}$ ) is the closest to the values for high-thermal-conductivity AlN.

Fig. 2 shows the theoretical LTCs of the  $\alpha$  and  $\beta$  phases as a function of  $T$ , in comparison with the reference experimental data, which were measured from the polycrystalline samples. The data of the polycrystalline bulk samples cannot be directly compared with the theoretical LTC tensors because the microstructures of the bulk samples affect the thermal conductivities. We calculate theoretical LTC values of the polycrystalline bulk sample as  $\kappa = w\kappa_{xx} + (1-w)\kappa_{zz}$ , with an adjustable parameter  $w$  between 0 and 1 for the least square differences from the experimental data.

The temperature dependence of the theoretical LTC, induced by  $\tau_{\text{ph-ph}}$ , is close to  $T^{-1}$  because 300 K is high enough to approximate the linewidth in Eq. (1) by a high-temperature limit for these phases. In Fig. 2-a, the temperature dependence of the experimental data of a chemically vapor-deposited  $\alpha\text{-Si}_3\text{N}_4$  sample<sup>37</sup> is deviated from  $T^{-1}$  considerably, intersecting the theoretical curves of the  $\kappa_{xx}$  and  $\kappa_{zz}$  at 400 and 600 K, respectively. Thus no value of  $w$  adjusts the theoretical LTC to the experimental curve. The full solution of LBTE would negligibly cure the disagreement. Including the simple phonon lifetime of boundary scattering,  $\tau_{\lambda,\text{bs}} = L/|\mathbf{v}_\lambda|$ , into the total phonon lifetime according to Matthiessen's rule, could not explain the discrepancy as well.  $\tau_{\lambda,\text{bs}} = L/|\mathbf{v}_\lambda|$  with  $L = 0.75 \mu\text{m}$ , which was much smaller than the experimental grain size  $10 \mu\text{m}$ , decreases the room-temperature theoretical  $\kappa_{xx}$  and  $\kappa_{zz}$  values toward the experimental value, but severely underestimated the experimental values at the high temperature side. At present, the reason for the discrepancy between the theoretical and experi-

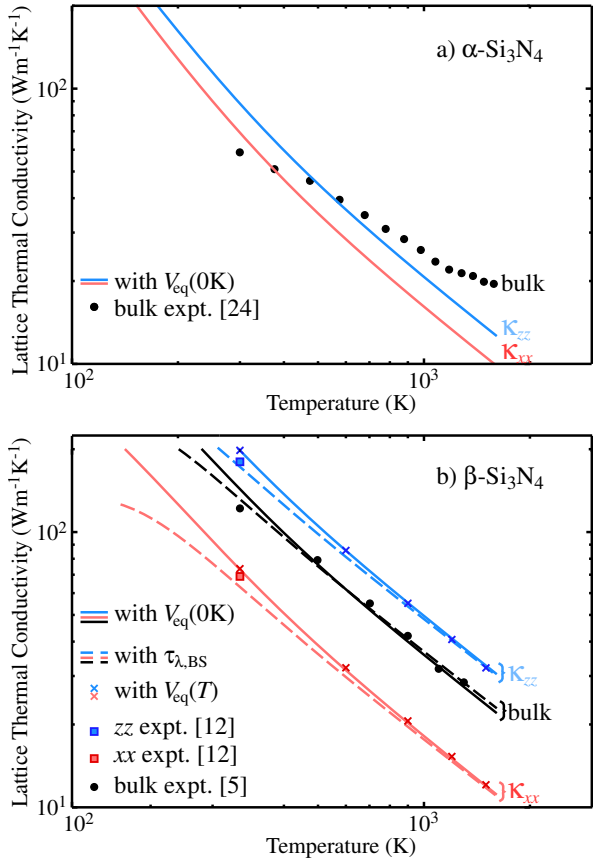


FIG. 2. (color online) Temperature dependence of LTC for  $\alpha$ - and  $\beta$ - $\text{Si}_3\text{N}_4$ . The LTC calculated with the fixed volume optimized at 0 K are shown by the solid curves. For  $\beta$ - $\text{Si}_3\text{N}_4$ , the LTC with the boundary scattering effect are shown by broken curves. The LTC calculated with the equilibrium volumes at the temperatures are shown by crosses. Theoretical LTC for the bulk  $\beta$ - $\text{Si}_3\text{N}_4$  sample are also shown to be compared with the experimental LTC (filled circles) of the bulk sample.

mental behaviors is unclear. Although the crystal structure of the experimental sample was characterized as  $\alpha$ - $\text{Si}_3\text{N}_4$ , significant lattice defects might exist in the as-deposited sample as pointed out by Hirosaki *et al.*<sup>16</sup>, and many of them might be diminished in the high temperature side of the measurement. The experimental values of the  $\beta$  phase ceramic bulk<sup>5</sup> in Fig. 2-b fall well between the calculated values of  $\kappa_{xx}$  and  $\kappa_{zz}$ . The experimental data are nearly parallel to the theoretical  $\kappa_{xx}$  and  $\kappa_{zz}$  curves. If we compare the experimental values with  $\sum_i \kappa_{ii}/3$ , which is a simple directional average, the calculation shows slight underestimations with respect to the experiment, which can be understood from an experimentally tailored microstructure containing large  $\beta$ - $\text{Si}_3\text{N}_4$  grains selectively grown along the  $c$  axis.<sup>5</sup>

The theoretical curve adjusted with  $w = 0.37$  explains well the experimental data of the poly-crystal bulk in Fig. 2-b. For the effects of lattice defects most of which are grain boundaries, we included  $\tau_{\lambda,\text{BS}}$  with  $L = 1 \mu\text{m}$  to

further fit the theoretical curve ( $w = 0.44$ ) to the experimental data. The  $L$  value is similar to the average grain size ( $2 \mu\text{m}$ ) of the experimental polycrystalline sample<sup>5</sup>. Fig. 2-b also contains the experimental  $\kappa_{xx}$  and  $\kappa_{zz}$  at room temperature by filled squares, which are in-between the theoretical components with and without  $\tau_{\lambda,\text{BS}}$ . The LTC values with the equilibrium lattice volumes ( $V_{\text{eq}}$ ) at 300, 600, 900, 1200 and 1500 K within QHA are plotted by crosses in Fig. 2. The deviations due to the thermal expansions were less than 1 %. Therefore this effect is negligible for the present study. The degree of the differences is similar to the case of Si and Ge<sup>36</sup>.

## B. Dispersion curves

Figure 3 shows the phonon band diagrams of the three  $\text{Si}_3\text{N}_4$  phases. The entire band diagrams are almost identical to those reported earlier<sup>39,40</sup>. However, here we focus on the group velocities on high-symmetry paths for the entire frequency range. This has not been investigated by the previous works.

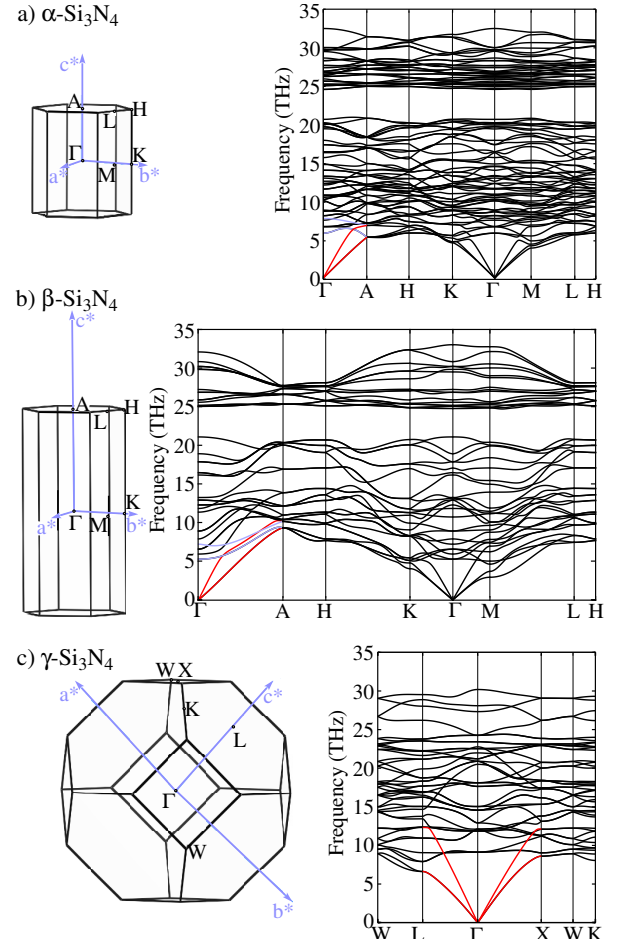


FIG. 3. (color online) Brillouin-zones (left) and calculated phonon band diagrams (right) for three  $\text{Si}_3\text{N}_4$  phases.

The acoustic branches in the  $\alpha$  phase highlighted in red along the  $\Gamma$ -A path in Fig. 3-a do not increase their frequencies much more than those along the other paths,  $\Gamma$ -K or  $\Gamma$ -M. The frequency maxima along the  $\Gamma$ -A path are around 7 THz, rather close to the maxima along the  $\Gamma$ -K and  $\Gamma$ -M paths (around 5 THz). The upper branches along the  $\Gamma$ -A path are also as flat as the upper branches along the  $\Gamma$ -K and  $\Gamma$ -M paths. In contrast, in the band diagram of the  $\beta$  phase (Fig. 3-b), the acoustic phonon branches highlighted in red along the  $\Gamma$ -A path increase their frequencies almost linearly from the  $\Gamma$ -point to the A-point and reach around 10 THz, along which the group velocity component  $v_{\lambda,z}$  maintains high values. This difference is because the  $\Gamma$ -A path length of the  $\beta$  phase is approximately half that of  $\alpha$ . The lattice constant  $c$  of  $\alpha$  is nearly twice that of  $\beta$ , owing to the difference in the stacking manner of the basal layers. Normally, optical branches are flat; however, the upper branches along the  $\Gamma$ -A path also have significantly large  $v_{\lambda,z}$ . In Fig. 3-c for the  $\gamma$  phase, the acoustic phonon branches highlighted in red show significant linear dispersion along the L- $\Gamma$ -X path. The frequencies of the longitudinal acoustic modes are 14 and 12.5 THz at the L- and X-points. The frequencies of the transverse acoustic modes are approximately half the values of the longitudinal modes at the L-point and a factor of  $1/\sqrt{2}$  smaller than the longitudinal modes at the X-point, as in the case of fcc rare gas solids<sup>41</sup>. The roughly constant gradients of the branches are large, reflecting the large elastic constants of the  $\gamma$  phase as shown in Table II.

### C. $\omega_\lambda$ counter map on reciprocal plane

The cross-sections of the phonon frequency distributions on the  $b^*$ - $c^*$  planes in the first Brillouin-zones are shown in Fig. 4. The cross-sections of other planes containing the  $c^*$  axis did not differ much from Fig. 4; thus, we focus on the results for the  $b^*$ - $c^*$  planes as representative of all such planes. We show only the frequencies of four modes from the lowest frequency because they contribute significantly to LTC. Fig. 4-a shows that the frequency distributions and group velocities of  $\alpha$ -Si<sub>3</sub>N<sub>4</sub> are fairly isotropic. On the other hand, in Fig. 4-b of the  $\beta$  phase, the iso-frequency lines in  $0.06 \leq q_{c^*} \leq 0.12$  ( $\text{\AA}^{-1}$ ) are rather parallel to the qb\* axis, indicating that the four modes of the  $\beta$  phase, in a significantly large part of the Brillouin zone, have group velocities oriented along the  $c$  axis.

### D. Frequency-dependences of $\kappa^c$ , $v_\lambda$ and $\Gamma_\lambda$

The microscopic phonon properties we have seen in the previous sections are located in specific paths or planes in the Brillouin zone. In order to more rigorously inspect the LTCs, we examine phonon properties taken over the Brillouin zone. As such properties, in Fig. 5 are shown

phonon densities of states (DOS), cumulative thermal conductivities and their frequency derivatives, weighted DOS with the squares of the group velocity components ( $v_{\lambda,x}$  and  $v_{\lambda,z}$ ), and finally, frequency distributions of linewidths

Firstly, we relate DOS (Fig. 5-a) with the cumulative thermal conductivity (Fig. 5-b). The 1st DOS peaks indicated by arrows are related to the flattening of the acoustic branches at the Brillouin zone boundaries. In  $\alpha$ - and  $\gamma$ -Si<sub>3</sub>N<sub>4</sub>, the phonons contributing to the LTCs are mainly located on the frequencies below the peaks, indicating that the main heat carriers are the phonons on the acoustic branches. In contrast, almost a half of the contributions to  $\kappa_{zz}$  in  $\beta$ -Si<sub>3</sub>N<sub>4</sub> are derived from the phonons above the peak, indicating that the low frequency optical phonons should contribute to this component significantly.

Secondly, in Figs. 5-b and c, the directional differences in the derivatives of the cumulative thermal conductivities in the  $\alpha$  and  $\beta$  phases are qualitatively well consistent with the directional differences in the weighted DOS. The relatively larger intensities in the weighted DOS with  $v_{\lambda,z}$  in  $\beta$ -Si<sub>3</sub>N<sub>4</sub>, critically causes the large anisotropy in its LTCs.

Fig. 5-d shows significantly similar linewidth distributions between the  $\alpha$  and  $\beta$  phases, which let the group velocities alone play the critical role on the different degrees of the anisotropy in the LTCs. Since it is curious that the linewidths are similar between these phases although their group velocities have marked differences, we investigate this similarity further. Recently Togo *et al.* have shown that the frequency distributions of the imaginary part of self-energy, which gives  $\Gamma_\lambda$  at  $\omega = \omega_\lambda$ , are mainly brought about by the three phonon selection rules.<sup>17</sup> Although the three-phonon interaction strength  $\Phi_{-\lambda\lambda'\lambda''}$  in Eq. (1) for the linewidths partly contains the selection rules (momentum conservation)<sup>17</sup>, we examine  $\Phi_{-\lambda\lambda'\lambda''}$  and the whole selection rules (momentum and energy conservation), one by one. In Table. xx,  $\Phi_{-\lambda\lambda'\lambda''}$  are compared as the averages over the frequency ranges between 0 and 15 THz and 0 and 35 THz. The values of the  $\alpha$  and  $\beta$  phases are very close to each other, indicating that  $\Phi_{-\lambda\lambda'\lambda''}$  have similar impacts on the linewidths of these phases.

In order to analyze the impacts of the selection rules on  $\Gamma_\lambda$ , we employ the joint density of states (JDOS)  $D_2(\mathbf{q}, \omega)$ ,

$$D_2(\mathbf{q}, \omega) = D_2^{(1)}(\mathbf{q}, \omega) + D_2^{(2)}(\mathbf{q}, \omega) \quad (4)$$

where

$$\begin{aligned} D_2^{(1)} &= \frac{1}{N} \sum_{\lambda'\lambda''} \Delta(-\mathbf{q} + \mathbf{q}' + \mathbf{q}'') \\ &\quad \times [\delta(\omega + \omega_{\lambda'} - \omega_{\lambda''}) + \delta(\omega - \omega_{\lambda'} + \omega_{\lambda''})], \\ D_2^{(2)} &= \frac{1}{N} \sum_{\lambda'\lambda''} \Delta(-\mathbf{q} + \mathbf{q}' + \mathbf{q}'') \\ &\quad \times \delta(\omega - \omega_{\lambda'} - \omega_{\lambda''}). \end{aligned}$$

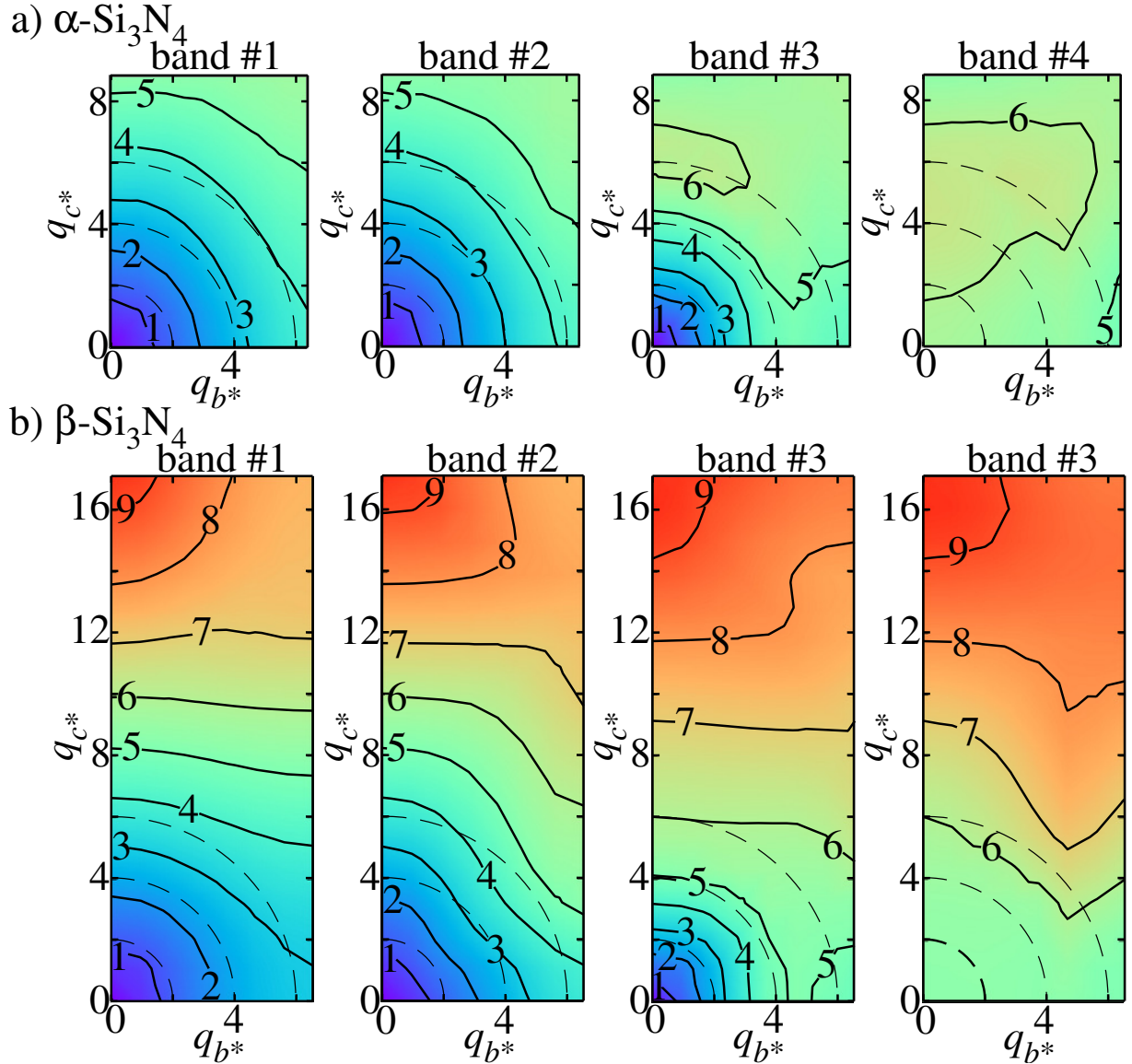


FIG. 4. (color online) Contour maps of phonon frequency (THz) on the  $b^*-c^*$  planes of Brillouin-zones. The maps for the four lowest-frequency phonon states are shown. The frequency landscapes are formed by simply connecting the frequencies of the same band indices, assigned by ascending order of frequency at the respective  $\mathbf{q}$  points.

Fig.xx shows the JDOS at three different  $\mathbf{q}$  points. Eq. (1) includes Bose-Einstein functions for the involved phonon modes and JDOS can be weighted with them as done in ref. SciRep and Togo, however we omit them for simplicity. With the weights, the absolute values are affected but the weighted JDOS of the  $\alpha$  and  $\beta$  phases are still similar. At the low frequency region responsible for the LTCs, among the two terms of  $D_2^{(1)}$  and  $D_2^{(2)}$  in Eq. (4), dominant is  $D_2^{(2)}$  which corresponds to the half part ( $\omega \geq 0$ ) of the auto-correlation function of DOS. The DOS of the  $\alpha$  and  $\beta$  phases in Fig. x-a commonly show the frequency gap. The auto-correlation functions,  $D_2^{(2)}$ , reflect this DOS feature, dropping suddenly around 0 THz and showing a small shoulder around

7 THz, which corresponds to the width of the gap. Moreover  $D_2^{(2)}$  shows a broad peak around 18 THz, which corresponds to the frequency shift to make the largest correlation between the higher and lower portions of DOS across the gap. Because the gap is basically originated from the differences in the vibrations of the planer NSi<sub>3</sub> commonly existing in the  $\alpha$  and  $\beta$  phases<sup>39</sup>, the major shapes of  $D_2^{(2)}$ , reflecting this gap feature, are similar in these phases. With the same origin, the JDOS of  $D_2^{(1)}$  are also similar in these phases. With these similar impacts of  $\Phi_{-\lambda\lambda'\lambda''}$  and JDOS on  $\Gamma_\lambda$ ,  $\Gamma_\lambda$  in Fig. xx-d are similar.

As a small but interesting difference in  $\Gamma_\lambda$  between these phases,  $\Gamma_\lambda$  below 5 THz in Fig. X-d are aligned on

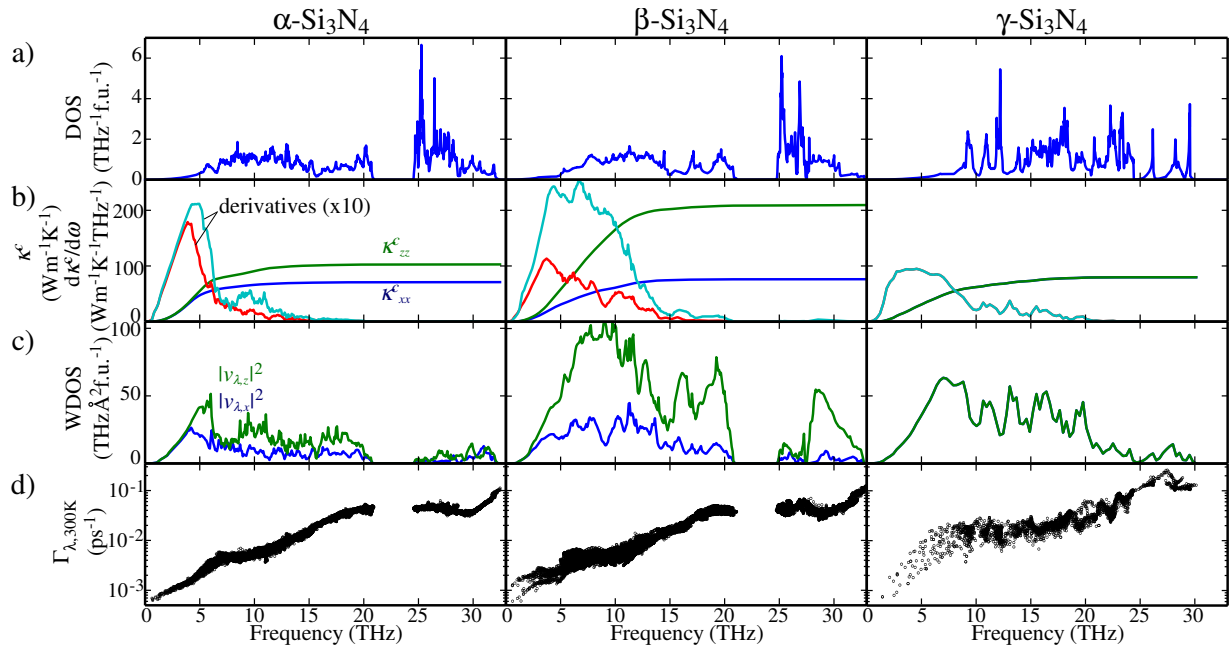


FIG. 5. (color online) Microscopic phonon properties of three  $\text{Si}_3\text{N}_4$  phases. Cumulative thermal conductivity  $\kappa^c$  and its derivative (a), DOS (b), DOS weighted by squared group velocity  $\langle v^2 \rangle$  (c), linewidth  $\Gamma$  (d), two factors composing linewidth (weighted joint density of states  $N$  (e) and average phonon-phonon interaction strength  $P$  (f)), and approximated linewidth  $\tilde{\Gamma}$  (g)

a smooth line in the  $\alpha$  phase, while those in the  $\beta$  phase are scattered roughly onto two different lines. This difference can be explained by the vibration directions shown in Fig. xxx. In Fig. xxx-a,  $\Gamma_\lambda$  are classified using colors according to the sums of the squares of the eigenvector components along  $q$ ; the sum is 1 for perfectly longitudinal waves. However, these sums have no clear contrast to distinguish the two branches in the  $\beta$  phase. Fig. xxx-b shows the same plot as Fig. xxx-a, but with colors according to the sums of the squares of the eigenvector components along the  $a$ - $b$  plane, which has 1 when the eigenvectors lie on the  $a$ - $b$  plane. There is a tendency in the  $\beta$  phase that  $\Gamma_\lambda$  are large for the vibrations along the  $a$ - $b$  plane. Therefore, within the single-mode RTA, for the phonon modes below 5 THz, all of which belong to the acoustic phonon branches, the vibration modes along the  $a$ - $b$  plane are more easily scattered in the  $\beta$  phase, no matter whether they are longitudinal or transverse. In Fig. xxxx-b-2 a straight line is drawn to divide the phonon modes into the two groups. The numbers of the phonon modes in the upper and lower parts are 357 and 126, whose ratio is reasonable as the population ratio of the vibration modes along the  $a$ - $b$  plane and out of the  $a$ - $b$  plane.

OOOOO To investigate the microscopic phonon-phonon interaction related to the thermal transport, we analyze the linewidths in Fig. 5-d. The linewidths of  $\alpha$ - and  $\beta$ - $\text{Si}_3\text{N}_4$  are similar to each other. They increase with frequency monotonically, containing a terrace at 6–8 THz. On the other hand, the linewidths of  $\gamma$ - $\text{Si}_3\text{N}_4$ ,

with a larger scattering in their values, more steeply increases until  $\sim 7$  THz and then stops increasing. The behavior is much different from those in  $\alpha$ - and  $\beta$ - $\text{Si}_3\text{N}_4$ . The marked difference is originated from the phase space available for three phonon scattering processes, showed in Fig. 5-e by the weighted joint density of states  $N_\lambda$ ,

Nevertheless the frequency dependences of the linewidths for all the polymorphs can be explained in terms of the phase space. Similar plateaus as in the linewidths are found at 6–8 THz for  $\alpha$ - and  $\beta$ - $\text{Si}_3\text{N}_4$  and above  $\sim 7$  THz for  $\gamma$ - $\text{Si}_3\text{N}_4$ . Additionally, the anharmonicity of the phonon modes in the same frequency-range as the linewidths is shown by the average phonon-phonon interaction strength  $P_\lambda$  in Fig. 5-f,

$$P_\lambda = \frac{1}{(3n_a)^2} \sum_{\lambda' \lambda''} |\Phi_{-\lambda \lambda' \lambda''}|^2. \quad (5)$$

The linewidths scatter more in the order of  $\alpha$ -,  $\beta$ -, and  $\gamma$ - $\text{Si}_3\text{N}_4$ .  $P_\lambda$  values scatter more in the same order. We can see that the overall shape of frequency-dependence of the linewidths is originated from the phase space represented by  $N_\lambda$ , while the scatter in the linewidth values comes from the anharmonicity as measured by  $P_\lambda$ . The approximated linewidths  $\tilde{\Gamma}_\lambda$  in Fig. 5-g, composed of the

products of  $N_\lambda$  and  $P_\lambda$ ,

$$\tilde{\Gamma}_\lambda = \frac{18\pi}{\hbar^2} P_\lambda N_\lambda, \quad (6)$$

may well show similar frequency-dependences to the linewidths as well. For quantitative comparison, the correlation coefficients between  $(\Gamma_\lambda, N_\lambda)$ ,  $(\Gamma_\lambda, P_\lambda)$ , and  $(\Gamma_\lambda, \tilde{\Gamma}_\lambda)$  spaces are (0.97, 0.92, and 0.54 for  $\alpha$ -,  $\beta$ -, and  $\gamma$ - $\text{Si}_3\text{N}_4$ , respectively), (0.94, 0.84 and 0.73) and (0.96, 0.92 and 0.71), respectively (See SM for details).

Although the values for  $\gamma$ - $\text{Si}_3\text{N}_4$  are much lower than the other two polymorphs, the behavior of the linewidths in the present systems are well characterized by  $N_\lambda$  and  $P_\lambda$ .

The outlines of the frequency-dependence of linewidths are very similar between  $\alpha$ - and  $\beta$ - $\text{Si}_3\text{N}_4$ . Thus the phonon lifetimes make small differences in their thermal conductivities. We can ascribe the anisotropy in their thermal conductivities to the group velocity components. In Fig. 5-c are shown the density of states weighted by the square of group velocity components along  $i = x$  and  $z$ , defined by

$$\langle v_i^2(\omega) \rangle = \frac{1}{N_\mathbf{q}\Omega} \int_0^\omega \sum_\lambda v_{\lambda,i}^2 \delta(\omega' - \omega) d\omega'. \quad (7)$$

The larger weights of squared group velocity components are distributed in low frequencies, as compared with the ordinal DOS (Fig. 5-b). The relative intensities of  $\langle v_z^2 \rangle$  and  $\langle v_x^2 \rangle$  in Fig. 5-c resemble the corresponding intensities of  $d\kappa_{zz}^c/d\omega$  and  $d\kappa_{xx}^c/d\omega$  in Fig. 5-a. This is an evidence for the relative degrees of the anisotropy in thermal transport of  $\alpha$ - and  $\beta$ - $\text{Si}_3\text{N}_4$  originating from the square of group velocity components.

For  $\gamma$ - $\text{Si}_3\text{N}_4$ , we can qualitatively deduce that mutual cancellation between the larger  $\Gamma_\lambda$  and  $\langle v^2 \rangle$  values suppresses  $\kappa^c$  to the value as small as  $\kappa_{xx}^c$  of  $\beta$ - $\text{Si}_3\text{N}_4$ .

## ACKNOWLEDGMENTS

The present work was partly supported by Grants-in-Aid for Scientific Research of MEXT, Japan (Grant No. 15K14108 and ESISM (Elements Strategy Initiative for Structural Materials) of Kyoto University).

## Appendix A: Pressure dependence of LTC of $\gamma$ -phase

\* k-tatsumi@imass.nagoya-u.ac.jp

- <sup>1</sup> G. Slack, Journal of Physics and Chemistry of Solids **34**, 321 (1973).
- <sup>2</sup> Y. Zhou, H. Hyuga, D. Kusano, Y.-i. Yoshizawa, and K. Hirao, Advanced Materials **23**, 4563 (2011).
- <sup>3</sup> K. Hirao, K. Watari, H. Hayashi, and M. Kitayama, MRS Bulletin **26**, 451 (2001).
- <sup>4</sup> K. Watari, Journal of the Ceramic Society of Japan **109**, S7 (2001).
- <sup>5</sup> N. Hirosaki, Y. Okamoto, M. Ando, F. Munakata, and Y. Akimune, Journal of the Ceramic Society of Japan **104**, 49 (1996).
- <sup>6</sup> F. L. Riley, Journal of the American Ceramic Society **83**, 245 (2000).
- <sup>7</sup> S. Hampshire, H. Park, D. Thompson, and K. Jack, Nature **274**, 880 (1978).
- <sup>8</sup> M. Yashima, Y. Ando, and Y. Tabira, The Journal of Physical Chemistry B **111**, 3609 (2007).
- <sup>9</sup> D. Du Boulay, N. Ishizawa, T. Atake, V. Streltsov, K. Furuya, and F. Munakata, Acta Crystallographica Section B: Structural Science **60**, 388 (2004).
- <sup>10</sup> A. Zerr, G. Miehe, G. Serghiou, M. Schwarz, E. Kroke, R. Riedel, H. Fueß, P. Kroll, and R. Boehler, Nature **400**, 340 (1999).
- <sup>11</sup> Y. Zhang, A. Navrotsky, and T. Sekine, Journal of materials research **21**, 41 (2006).
- <sup>12</sup> B. Li, L. Pottier, J. Roger, D. Fournier, K. Watari, and K. Hirao, Journal of the European Ceramic Society **19**, 1631 (1999).
- <sup>13</sup> T. Takahashi, M. Sado, N. Sugimoto, J. Tatami, M. Iijima, S. Inagaki, Y. Kubota, I. Yamamoto, and S. Tanaka, Advanced Powder Technology **27**, 2005 (2016).

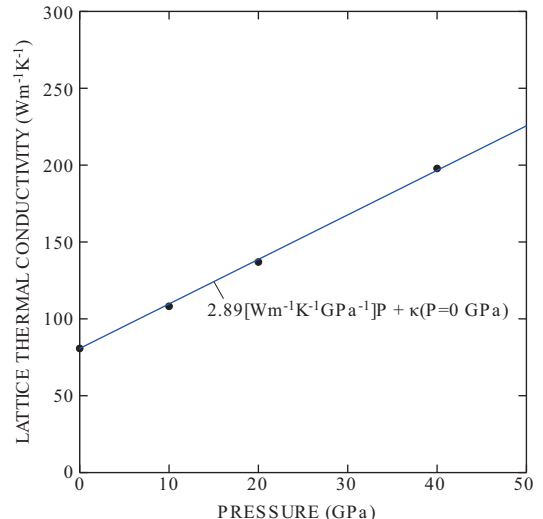


FIG. 6. (color online) Pressure dependence of LTC of  $\gamma$ - $\text{Si}_3\text{N}_4$ .

- <sup>14</sup> Y. Yamamoto, N. Hirosaki, I. Ishikawa, J. YE, K. Matsuo, K. Furuya, F. Munakata, and Y. Akimune, Journal of the Ceramic Society of Japan **108**, 515 (2000).
- <sup>15</sup> K. Watari, L. Pottier, B. Li, D. Fournier, and M. Toriyama, Ceramic Transactions(USA) **118**, 341 (2000).

- <sup>16</sup> N. Hirosaki, S. Ogata, C. Kocer, H. Kitagawa, and Y. Nakamura, Physical Review B **65**, 134110 (2002).
- <sup>17</sup> A. Togo, L. Chaput, and I. Tanaka, Physical Review B **91**, 094306 (2015).
- <sup>18</sup> D. Morelli and J. Heremans, Applied physics letters **81**, 5126 (2002).
- <sup>19</sup> L. Chaput, Physical review letters **110**, 265506 (2013).
- <sup>20</sup> S.-i. Tamura, Physical Review B **27**, 858 (1983).
- <sup>21</sup> A. Togo and I. Tanaka, Scripta Materialia **108**, 1 (2015).
- <sup>22</sup> P. E. Blöchl, Phys. Rev. B **50**, 17953 (1994).
- <sup>23</sup> G. Kresse and J. Furthmüller, Physical review B **54**, 11169 (1996).
- <sup>24</sup> G. Kresse, J. Non-Cryst. Solids **193**, 222 (1995).
- <sup>25</sup> D. J. Kresse, Georg, Phys. Rev. B **59**, 1758 (1999).
- <sup>26</sup> J. P. Perdew, K. Burke, and M. Ernzerhof, Physical review letters **77**, 3865 (1996).
- <sup>27</sup> W. Paszkowicz, R. Minikayev, P. Piszora, M. Knapp, C. Bähtz, J. Recio, M. Marques, P. Mori-Sánchez, L. Gerward, and J. Jiang, Physical Review B **69**, 052103 (2004).
- <sup>28</sup> D. M. Ceperley and B. Alder, Physical Review Letters **45**, 566 (1980).
- <sup>29</sup> S. Wei and M. Chou, Physical review letters **69**, 2799 (1992).
- <sup>30</sup> M. T. Dove, Introduction to lattice dynamics, Vol. 4 (Cambridge university press, 1993) pp. 76–77.
- <sup>31</sup> P. P. M. K. R. Minikayev, W. Paszkowicz and C. Bähtz, “Thermal expansion of and silicon nitride,” (2007).
- <sup>32</sup> P. Andersson, Journal of Physics C: Solid State Physics **18**, 3943 (1985).
- <sup>33</sup> A. Cepellotti and N. Marzari, Physical Review X **6**, 041013 (2016).
- <sup>34</sup> R. J. Hardy, Physical Review B **2**, 1193 (1970).
- <sup>35</sup> S. Mukhopadhyay, L. Lindsay, and D. J. Singh, Scientific reports **6** (2016).
- <sup>36</sup> A. Ward and D. Broido, Physical Review B **81**, 085205 (2010).
- <sup>37</sup> T. Hirai, S. Hayashi, and K. Niihara, AM. CERAM. SOC. BULL. Am. Ceram. Soc. Bull. **57**, 1126 (1978).
- <sup>38</sup> G. A. Slack, R. A. Tanzilli, R. Pohl, and J. Vandersande, Journal of Physics and Chemistry of Solids **48**, 641 (1987).
- <sup>39</sup> A. Kuwabara, K. Matsunaga, and I. Tanaka, Physical Review B **78**, 064104 (2008).
- <sup>40</sup> B. Xu, J. Dong, P. F. McMillan, O. Shebanova, and A. Salamat, Physical Review B **84**, 014113 (2011).
- <sup>41</sup> M. T. Dove, Introduction to lattice dynamics, Vol. 4 (Cambridge university press, 1993) pp. 30–31.